

Optical Chirality of Time-Harmonic Wavefields for Classification of Scatterers

Philipp Gutsche^{1,2,*} and Manuel Nieto-Vesperinas³

¹Freie Universität Berlin, Mathematics Institute, Berlin, 14195, Germany

²Zuse Institute Berlin, Computational Nano Optics, Berlin, 14195, Germany

³Instituto de Ciencia de Materiales de Madrid, Consejo Superior de Investigaciones Científicas, Madrid, 28049, Spain

*gutsche@zib.de

January 19, 2022

Abstract

We derive expressions for the scattering, extinction and conversion of the chirality of monochromatic light scattered by bodies which are characterized by a T -matrix. In analogy to the conditions obtained from the conservation of energy, these quantities enable the classification of arbitrary scattering objects due to their full, i.e. either chiral or achiral, electromagnetic response. To this end, we put forward and determine the concepts of duality and breaking of duality symmetry, anti-duality, helicity variation, helicity annihilation and the breaking of helicity annihilation. Different classes, such as chiral and dual scatterers, are illustrated in this analysis with model examples of spherical and non-spherical shape. As for spheres, these concepts are analysed by considering non-Rayleigh dipolar dielectric particles of high refractive index, which, having a strong magnetic response to the incident wavefield, offer an excellent laboratory to test and interpret such changes in the chirality of the illumination. In addition, comparisons with existing experimental data are made.

Introduction

Progress in designing spatially structured electromagnetic wavefields [1] is giving rise to an increasing interest in electromagnetic waves with twists of their polarization and wavefronts, i.e. with spin and orbital angular momenta [2, 3, 4]. This complex shaped light is receiving substantial attention because of its potential for probing light-matter interactions, with additional information contents like in new circular dichroism (CD) techniques in chiroptical spectroscopy [5, 6] and spin-orbit phenomena [7, 8, 9, 10], including Hall effects [11, 12]. Additionally, such fields with angular momentum are of potential importance as communication vehicles with larger numbers of degrees of freedom [13, 14, 15].

Considering light as a probe, the relationship between its chirality and that of matter is of great importance in the understanding of their mutual interactions [16, 17]. Related magnetoelectric effects associated with the breaking of dual, P- and T-symmetries have been studied [18]. However, procedures that enhance energy transfer (e.g. Förster resonance energy transfer, FRET) between molecules [19] and CD measurements are often hindered by very weak signals. The sensitivity of such experiments is enhanced by increasing the helicity of the illuminating field [20, 21], using either particles with plasmon resonances [22, 23, 24, 25] or magneto-dielectric particles [26], or by means of near-field hot spots between plasmonic nanoparticles on tailoring the incident polarization [27]. Further strategies for strong chiroptical effects include thermally-controlled chirality in hybrid THz metamaterials [28] and enhancing the interference of electric and magnetic dipoles of the excited molecule [29].

In recent work, we established consequences of the continuity equation that governs the conservation of electromagnetic chirality of light and other electromagnetic waves [30, 31, 32]. In this way, we introduced an optical theorem which describes the extinction of helicity of time-harmonic wavefields on scattering and absorption by arbitrary scatterers [33] and that shows the connections between the chirality of the illuminating wave and that of the scattering object. This yields a unified formulation of CD [17, 34] and enables the introduction of a chirality enhancement factor [34, 35] which is the chiral analogue of the Purcell factor for the emitted energy from nanostructures in inhomogeneous environments. In addition, the continuity equation of chirality conservation was extended to twisted fields near nanostructures, as well as to arbitrary configurations [36, 37]. We emphasize that the optical chirality of monochromatic, i.e. time-harmonic, fields addressed in this work is equivalent to their helicity [32, 17]. Both scalars differ only by a

Original Version: Gutsche, P. & Nieto-Vesperinas, M. Optical Chirality of Time-Harmonic Wavefields for Classification of Scatterers. Sci. Rep. **8**, 9416 (2018). <https://doi.org/10.1038/s41598-018-27496-w>

factor which is the square of the wavenumber [33]. Since the former quantity has been extensively used in the literature after Ref. [20], we employ both terms interchangeably.

In this paper, we start from these concepts to classify the optical response of nanoparticles to monochromatic wavefields. These isolated scatterers are well described by their T -matrix [38]. In analogy, and complementary, to the T -matrix based standard classification of scatterers into lossless and lossy particles [39], we now propose an analysis stemming from the variation of helicity of chiral illuminating fields, which characterizes the major changes in the helicity of the incident wave with respect to that of the scattered field. To this end, we first establish the chiral quantities for this general formulation, and develop a matrix-based formalism for the illumination with light of well-defined helicity [40]. Then we put forward scalars which provide insight into the variation of incident circular polarization, including breakings of duality, anti-duality, annihilation of helicity, as well as the helicity variation. These concepts allow us to establish the following three classes of scattering bodies: helicity-keeping and helicity-flipping scatterers, which are weaker forms of dual and anti-dual bodies, respectively. The third class which we introduce is that of helicity-annihilating particles.

Our findings are first illustrated by numerical studies of spherical objects described by Mie theory. We thus start by addressing a magneto-dielectric, dipolar in the broad sense [34] (i.e. non-Rayleigh) silicon nanoparticle, as well as an isotropic chiral one built from it. As we shall show, the existence of a strongly induced magnetic dipole, in addition to the usual electric one, confers unique characteristics to this kind of scatterer as regards the rich variety of effects that it causes in the incident field chirality. Phenomena that, in turn, constitute signatures of the body magnetodielectric properties. Finally, the chiroptical behaviour of anisotropic particles is discussed with these novel quantities, studying both an achiral ellipsoidal-shaped body and a gold nanoparticle which was experimentally investigated before [41].

Results

T -Matrix Formalism

The electromagnetic response of a scattering object to an external illumination in an extinction experiment, i.e. scattering plus absorption or conversion, can be described by a matrix T which gives the relation of the incident and scattered fields, \mathbf{i} and \mathbf{s} respectively[38]: $T \cdot \mathbf{i} = \mathbf{s}$.

For isolated scatterers, vector spherical harmonics (VSHs) $\mathbf{M}^{(l)}$ and $\mathbf{N}^{(l)}$ ($l = 1, 3$) are a suitable basis. VSHs are rigorous solutions of Maxwell's equations and there are two distinct classes. In one class are the incident fields (\mathbf{p}, \mathbf{q}) , the other class (\mathbf{a}, \mathbf{b}) pertains to the scattered fields which obey the radiation condition. Accordingly, the incident electric \mathcal{E}_{inc} and magnetic \mathcal{H}_{inc} time-harmonic fields are given by [42, Sec. 9.7]

$$\mathcal{E}_{\text{inc}}(\mathbf{x}, t) = e^{-i\omega t} \sum_{m=1}^{\infty} \sum_{n=-m}^{n=m} p_{mn} \mathbf{N}_{mn}^{(1)}(\mathbf{x}) + q_{mn} \mathbf{M}_{mn}^{(1)}(\mathbf{x}), \quad \mathcal{H}_{\text{inc}}(\mathbf{x}, t) = -\frac{i}{Z} e^{-i\omega t} \sum_{m=1}^{\infty} \sum_{n=-m}^{n=m} p_{mn} \mathbf{M}_{mn}^{(1)}(\mathbf{x}) + q_{mn} \mathbf{N}_{mn}^{(1)}(\mathbf{x}) \quad (1)$$

with the wave impedance $Z = \sqrt{\mu_0 \mu / (\epsilon_0 \epsilon)}$. While the scattered fields are

$$\mathcal{E}_{\text{sca}}(\mathbf{x}, t) = e^{-i\omega t} \sum_{m=1}^{\infty} \sum_{n=-m}^{n=m} a_{mn} \mathbf{N}_{mn}^{(3)}(\mathbf{x}) + b_{mn} \mathbf{M}_{mn}^{(3)}(\mathbf{x}), \quad \mathcal{H}_{\text{sca}}(\mathbf{x}, t) = -\frac{i}{Z} e^{-i\omega t} \sum_{m=1}^{\infty} \sum_{n=-m}^{n=m} a_{mn} \mathbf{M}_{mn}^{(3)}(\mathbf{x}) + b_{mn} \mathbf{N}_{mn}^{(3)}(\mathbf{x}). \quad (2)$$

The index m indicates the multipole order and it is associated to the eigenvalue $m(m+1)$ of the squared orbital angular momentum operator L^2 in the spherical harmonic basis $Y_{mn}(\theta, \phi)$ [42, Sec. 9.7] (θ and ϕ being the polar and azimuthal angles of the position vector \mathbf{x}). The series above will be truncated at an order M in the following calculations. The index $|n| < m$ is related to the azimuthal behaviour of the VSHs. The VSHs $\mathbf{N}_{mn}^{(3)}$ and $\mathbf{M}_{mn}^{(3)}$ are proportional to the electric and magnetic outgoing multipolar fields, respectively. On the other hand, the VSHs $\mathbf{N}_{mn}^{(1)}$ and $\mathbf{M}_{mn}^{(1)}$ of the source-free incident wave are proportional to the electric and magnetic multipolar fields with both outgoing and incoming components [43]. Because of this, (1) and (2) represent the incident and scattered fields in the *parity basis*, namely that of eigenmodes of electric and magnetic nature.

In matrix notation, the coefficients of the series expansions (1) and (2) are related to each other through the T -matrix [44, 38]:

$$T \begin{pmatrix} \mathbf{p} \\ \mathbf{q} \end{pmatrix} = \begin{pmatrix} T_{ee} & T_{me} \\ T_{em} & T_{mm} \end{pmatrix} \begin{pmatrix} \mathbf{p} \\ \mathbf{q} \end{pmatrix} = \begin{pmatrix} \mathbf{a} \\ \mathbf{b} \end{pmatrix}, \quad (3)$$

where T has been subdivided into electric T_{ee} , magnetic T_{mm} and cross electric-magnetic T_{em}, T_{me} matrices.

The scattering solution for isotropic spherical particles with relative permittivity ϵ and relative permeability μ are given analytically [45]. Furthermore, if the sphere is optically active, the refractive indices differ for right and left circularly polarized illumination, being n_R and n_L , respectively. Using the achiral refractive index $n = \sqrt{\epsilon \mu}$ and assuming that particle is reciprocal, its optical behaviour is described with the Pasteur, or chirality, parameter $\kappa \in [-1, 1]$ [46, Eq. (2.85)] as $n_R = n(1 + \kappa)$ and $n_L = n(1 - \kappa)$.

For a geometrically isotropic sphere, the respective submatrices of the T -matrix in (3) are diagonal. In the case of reciprocal materials, we have additionally $T_{em} = T_{me}$. The main diagonal elements of T_{ee} , T_{mm} and T_{em} are given in the Methods section.

Energy Conservation

Assuming the scatterer is embedded in a lossless medium, the conservation of energy predicts a scattered W_{sca} , extinction W_{ext} and absorption W_{abs} of energy related by $W_{\text{ext}} = W_{\text{sca}} + W_{\text{abs}}$. In the VSH basis, these quantities are reduced to the following expressions [38, Eq. (5.18a, 5.18b)]. Note that our notation for the role of (\mathbf{p}, \mathbf{q}) and (\mathbf{a}, \mathbf{b}) is interchanged with respect to that of Ref. [38], using instead that of Ref. [47]. For the sake of brevity, we henceforth omit the variation ranges of the indices m and n in the series representations and obtain

$$W_{\text{sca}} = \frac{1}{2k^2 Z} \sum_{mn} |a_{mn}|^2 + |b_{mn}|^2 = \frac{1}{2k^2 Z} (|\mathbf{a}|^2 + |\mathbf{b}|^2), \quad (4)$$

$$W_{\text{ext}} = -\frac{1}{2k^2 Z} \sum_{mn} \text{Re}(p_{mn}^* a_{mn} + q_{mn}^* b_{mn}) = \frac{1}{2k^2 Z} \frac{1}{2} (\mathbf{p}^H \mathbf{a} + \mathbf{q}^H \mathbf{b} + \mathbf{a}^H \mathbf{p} + \mathbf{b}^H \mathbf{q}), \quad (5)$$

where H denotes the Hermitian adjoint, i.e. matrix transposition and complex conjugation, and $k = n_s \omega / c_0$ is the wavenumber, with n_s being the refractive index of the embedding medium. Since we use normalized VSHs, here and in the following we drop the terms $|\mathbf{N}_{mn}|^2 = |\mathbf{M}_{mn}|^2 = 1(V/m)^2$. Taking this unity factor and its dimension into account, the unit of the integrated energy fluxes W_{sca} and W_{ext} is watt, as expected. Eqs. (4) and (5) may be written as

$$2k^2 Z W_{\text{sca}} = (\mathbf{p}^H \mathbf{q}^H) T^H T \begin{pmatrix} \mathbf{p} \\ \mathbf{q} \end{pmatrix} = (\mathbf{p}^H \mathbf{q}^H) \mathbb{W}_{\text{sca}} \begin{pmatrix} \mathbf{p} \\ \mathbf{q} \end{pmatrix}, \quad (6)$$

$$2k^2 Z W_{\text{ext}} = -(\mathbf{p}^H \mathbf{q}^H) \frac{1}{2} (T^H + T) \begin{pmatrix} \mathbf{p} \\ \mathbf{q} \end{pmatrix} = (\mathbf{p}^H \mathbf{q}^H) \mathbb{W}_{\text{ext}} \begin{pmatrix} \mathbf{p} \\ \mathbf{q} \end{pmatrix}. \quad (7)$$

The quadratic matrices \mathbb{W}_{sca} and \mathbb{W}_{ext} have dimension $2M(M+2)$ for multipole orders $m = 1, \dots, M$. From the conservation of energy, the following conditions apply [39, Eq. (10)]

$$\text{Lossless scatterer: } \mathbb{W}_{\text{ext}} = \mathbb{W}_{\text{sca}}, \quad (8)$$

$$\text{Lossy scatterer: } (\mathbb{W}_{\text{ext}} - \mathbb{W}_{\text{sca}}) \text{ is HPD}, \quad (9)$$

where HPD means Hermitian positive definite. Note that both \mathbb{W}_{sca} and \mathbb{W}_{ext} are Hermitian by construction. These general matrices provide the illumination-independent information on scattering and extinction of energy by an isolated scatterer whose optical response is described by its T -matrix. Eq. (6) indicates that multiplying \mathbb{W}_{sca} on the left and right with the vector of coefficients (\mathbf{p}, \mathbf{q}) of the incident light gives the scalar scattered energy W_{sca} , for the specific illumination with (\mathbf{p}, \mathbf{q}) . The same holds for the matrix \mathbb{W}_{ext} and the energy W_{ext} extinguished from the incident field [cf. Eq. (7)] as well as for the matrices \mathbb{X}_{sca} and \mathbb{X}_{ext} , which represent the scattered and extinguished optical chirality and are introduced in (12) and (13) below.

Chirality Conservation

The conservation law of optical chirality [36, 33] states that the scattered chirality X_{sca} and the extinguished chirality (or chirality extinction) X_{ext} , as well as the converted chirality (or chirality conversion) X_{conv} are related by $X_{\text{ext}} = X_{\text{sca}} + X_{\text{conv}}$. Note that as shown in Ref. [36] X_{conv} is a field chirality that may be either absorbed or generated on scattering of the incident wave by the body. This is why it is named **chirality conversion**.

The optical chirality density in the near-field is proportional to the excitation rate of chiral molecules [20]. Here, we study the integrated optical chirality flux density yielding extinction X_{ext} and scattered X_{sca} chirality, as well as its conversion X_{conv} . The scattered optical chirality flux *density* is proportional to the difference of the circular polarization components of the scattered field at a specific point in space, thus being the third Stokes parameter. Its *integral*, the scattered chirality X_{sca} , is the angular average of the differential circular polarization of scattering. That is, $X_{\text{sca}} = 0$ both for locally achiral light (e.g. linearly polarized plane waves), as well as for light sources which emit equal parts of right and left circular polarization in different directions (e.g. circularly polarized electric dipoles).

In order to classify the chiroptical response of isolated scatterers, we henceforth establish these quantities in the VSH basis:

$$X_{\text{sca}} = \frac{1}{2kZ} \sum_{mn} 2 \text{Re}(a_{mn}^* b_{mn}) = \frac{1}{2kZ} (\mathbf{a}^H \mathbf{b} + \mathbf{b}^H \mathbf{a}), \quad (10)$$

$$X_{\text{ext}} = -\frac{1}{2kZ} \sum_{mn} \text{Re}(p_{mn}^* b_{mn} + q_{mn}^* a_{mn}) = -\frac{1}{2kZ} \frac{1}{2} (\mathbf{p}^H \mathbf{b} + \mathbf{q}^H \mathbf{a} + \mathbf{b}^H \mathbf{p} + \mathbf{a}^H \mathbf{q}). \quad (11)$$

And they may also be written as

$$2kZX_{\text{sca}} = (\mathbf{p}^H \mathbf{q}^H) \begin{pmatrix} T_{ee}^H T_{em} + T_{em}^H T_{ee} & T_{ee}^H T_{mm} + T_{em}^H T_{me} \\ T_{mm}^H T_{ee} + T_{me}^H T_{em} & T_{me}^H T_{mm} + T_{mm}^H T_{me} \end{pmatrix} \begin{pmatrix} \mathbf{p} \\ \mathbf{q} \end{pmatrix} = (\mathbf{p}^H \mathbf{q}^H) \mathbb{X}_{\text{sca}} \begin{pmatrix} \mathbf{p} \\ \mathbf{q} \end{pmatrix}, \quad (12)$$

$$2kZX_{\text{ext}} = -(\mathbf{p}^H \mathbf{q}^H) \frac{1}{2} \begin{pmatrix} T_{em} + T_{em}^H & T_{ee}^H + T_{mm} \\ T_{ee} + T_{mm}^H & T_{me} + T_{me}^H \end{pmatrix} \begin{pmatrix} \mathbf{p} \\ \mathbf{q} \end{pmatrix} = (\mathbf{p}^H \mathbf{q}^H) \mathbb{X}_{\text{ext}} \begin{pmatrix} \mathbf{p} \\ \mathbf{q} \end{pmatrix}. \quad (13)$$

Incident Light of Well-Defined Helicity

Of particular interest are wavefields of well-defined helicity [48], i.e. those whose plane wave components [31, 34] all have the same helicity handedness of circular polarization with respect to their wavevector. In the following, we discuss the helicity of the incident light which is given by the VSH coefficients (\mathbf{p}, \mathbf{q}) in (1).

The transformation [40, 49, 50]:

$$\mathbf{A}_{nm}^{(1\pm)}(\mathbf{x}) = \frac{\mathbf{N}_{mn}^{(1)}(\mathbf{x}) \pm \mathbf{M}_{mn}^{(1)}(\mathbf{x})}{\sqrt{2}}, \quad (14)$$

changes the representation (1) of the incident wavefield in the parity basis to the *helicity basis* in which they have positive [sign + in (14)] or negative [sign - in (14)] *well-defined helicity*.

In this framework, the conditions for fields of well-defined helicity may be straightforwardly derived from the relation of the integrated energy and chirality introduced in the previous section. The incident energy is $2k^2ZW_{\text{inc}} = |\mathbf{p}|^2 + |\mathbf{q}|^2$ [cf. (4) replacing (\mathbf{a}, \mathbf{b}) by (\mathbf{p}, \mathbf{q})], whereas the incident chirality is $2kZX_{\text{inc}} = 2\text{Re}(\mathbf{p}^* \cdot \mathbf{q})$ [cf. (10)].

For incident fields of well-defined helicity, it is required that $X_{\text{inc}} = \pm kW_{\text{inc}}$, where as in (14) the sign \pm denotes a state of positive and negative helicity, respectively. Accordingly, a positive helicity state requires that $\mathbf{q} = \mathbf{p}$ and a negative helicity state is characterized by $\mathbf{q} = -\mathbf{p}$. Notice that both conditions are independent of each other, so that the coefficients of a positive helicity state are not related to those of a negative helicity state. That is why we denote \mathbf{p}^+ and \mathbf{p}^- the coefficients of an arbitrary field of well-defined positive and negative helicity, respectively. Summarizing, it holds either $\mathbf{q}^+ = \mathbf{p}^+$ or $\mathbf{q}^- = -\mathbf{p}^-$ for incident light of well-defined positive or negative helicity, respectively.

Therefore here and throughout the entire paper, the superscripts \pm denote illumination with light of well-defined helicity. In what follows, we shall analyze the response of an arbitrary scatterer to incident light of either positive or negative helicity. Specifically, we investigate the scattered energy W_{sca}^+ or W_{sca}^- , as well as the scattered chirality X_{sca}^\pm , for illuminating light of positive or negative helicity, respectively.

For $2k^2ZW_{\text{sca}}^\pm = (\mathbf{p}^\pm)^H \mathbb{W}_{\text{sca}}^\pm \mathbf{p}^\pm$ and $2kZX_{\text{sca}}^\pm = (\mathbf{p}^\pm)^H \mathbb{X}_{\text{sca}}^\pm \mathbf{p}^\pm$, one has that

$$\mathbb{W}_{\text{sca}}^\pm = + \left\{ (T_e^\pm)^H T_e^\pm + (T_m^\pm)^H T_m^\pm \right\}, \quad (15)$$

$$\mathbb{X}_{\text{sca}}^\pm = \pm \left\{ (T_m^\pm)^H T_e^\pm + (T_e^\pm)^H T_m^\pm \right\}, \quad (16)$$

where $T_e^\pm = T_{ee} \pm T_{me}$ and $T_m^\pm = T_{mm} \pm T_{em}$. For $2k^2ZW_{\text{ext}}^\pm = (\mathbf{p}^\pm)^H \mathbb{W}_{\text{ext}}^\pm \mathbf{p}^\pm$ and $2kZX_{\text{ext}}^\pm = (\mathbf{p}^\pm)^H \mathbb{X}_{\text{ext}}^\pm \mathbf{p}^\pm$, it holds

$$\mathbb{W}_{\text{ext}}^\pm = \pm \mathbb{X}_{\text{ext}}^\pm = -\frac{1}{2} \left\{ T_e^\pm + (T_e^\pm)^H + T_m^\pm + (T_m^\pm)^H \right\}. \quad (17)$$

For randomly oriented isolated scatterers, averaging over all illumination directions is of interest. This is because in dilute solutions, where multiple scattering can be neglected, the experimental results are dominated by the averaged response of a single particle [41]. Let $W_{\text{ext}}^\pm(\theta, \phi)$ be the energy extinction of an incident circularly (\pm) -polarized (CPL) plane wave with propagation direction given by θ and ϕ . From the expansion of plane waves into vector spherical harmonics [38, Eq. (C57)], one derives that the averaged energy extinction is given by

$$\overline{W_{\text{ext}}^\pm} = \frac{1}{2\pi^2} \int \int W_{\text{ext}}^\pm(\theta, \phi) d\theta d\phi = \frac{\pi}{k^2 Z} \sum_{ii} (\mathbb{W}_{\text{ext}}^\pm)_{ii}, \quad (18)$$

where $(\mathbb{W}_{\text{ext}}^\pm)_{ii}$ are the diagonal elements of the extinction energy matrices of well-defined helicity states (17). Similarly, it follows

$$\overline{W_{\text{sca}}^\pm} = \frac{\pi}{k^2 Z} \sum_{ii} (\mathbb{W}_{\text{sca}}^\pm)_{ii}, \quad \overline{X_{\text{sca}}^\pm} = \frac{\pi}{kZ} \sum_{ii} (\mathbb{X}_{\text{sca}}^\pm)_{ii}, \quad \overline{X_{\text{ext}}^\pm} = \frac{\pi}{kZ} \sum_{ii} (\mathbb{X}_{\text{ext}}^\pm)_{ii}. \quad (19)$$

Definitions for Classification of Scatterers

Duality and Anti-Duality

The scattered field of a **dual** scatterer has the same (well-defined) helicity as the incident field, i.e. $X_{\text{sca}}^+ = kW_{\text{sca}}^+$ for positive incident helicity, and $X_{\text{sca}}^- = -kW_{\text{sca}}^-$ for negative incident helicity. In matrix notation, it follows $\mathbb{X}_{\text{sca}}^\pm \mp \mathbb{W}_{\text{sca}}^\pm =$

$(T_e^\pm - T_m^\pm)^H (T_e^\pm - T_m^\pm) = 0$. In general, we establish the **duality breaking** $\mathcal{d} \in [0, 1]$ of the scattering object with an arbitrary matrix norm $||\cdot||$ as

$$\mathcal{d} = \max_{\pm} \left(\frac{||T_e^\pm - T_m^\pm||}{||T_e^\pm|| + ||T_m^\pm||} \right). \quad (20)$$

Our formalism is independent of the choice of the specific norm. Due to its numerical robustness, we choose the 2-norm $||A||_2$ of a matrix A which is given by the largest singular value of A . Note in this connection that if the Frobenius norm were chosen in Eq. (20), \mathcal{d} would be similar to the definition established in [47, Eq. (23)], [51, Eq. (32)] and [52, Eq. (2)].

On the other hand, if the scattered field has the opposite (well-defined) helicity with respect to that of the incident field, i.e. $X_{\text{sca}}^+ = -kW_{\text{sca}}^+$ for positive incident helicity and $X_{\text{sca}}^- = kW_{\text{sca}}^-$ for negative incident helicity, we shall say that the scatterer is **anti-dual**. In matrix notation, it follows $\mathbb{X}_{\text{sca}}^\pm \pm \mathbb{W}_{\text{sca}}^\pm = (T_e^\pm + T_m^\pm)^H (T_e^\pm + T_m^\pm) = 0$. Thus, in general, we herewith put forward the **anti-duality breaking** $\mathcal{d} \in [0, 1]$ as

$$\mathcal{d} = \max_{\pm} \left(\frac{||T_e^\pm + T_m^\pm||}{||T_e^\pm|| + ||T_m^\pm||} \right). \quad (21)$$

Helicity Variation

Given an incident field of well-defined helicity, in general the helicity of the scattered field may have the same sign as the incident one but may not be well-defined, i.e. its angular spectrum of plane wave components [31, 34] is composed of some with positive and some with negative helicity. If X_{sca} has the same sign as that of the incident field (e.g. $X_{\text{sca}}^+ > 0$ for positive incident helicity), we put forward the term **helicity-keeping** classifying such scatterers. By contrast, a **helicity-flipping** scatterer (e.g. $X_{\text{sca}}^+ < 0$ for positive incident helicity) changes the sign of the incident helicity to its opposite value. If an incident chiral field is scattered into a purely achiral field with $X_{\text{sca}}^\pm = 0$, we shall call the scatterer **helicity-annihilating**. Therefore, we establish the following classification of scattering bodies:

$$\text{Perfectly Helicity-Keeping: } \mathbb{X}_{\text{sca}}^+ \text{ (HPD) and } \mathbb{X}_{\text{sca}}^- \text{ (HND)}, \quad (22)$$

$$\text{Perfectly Helicity-Flipping: } \mathbb{X}_{\text{sca}}^+ \text{ (HND) and } \mathbb{X}_{\text{sca}}^- \text{ (HPD)}, \quad (23)$$

$$\text{Perfectly Helicity-Annihilating: } \mathbb{X}_{\text{sca}}^\pm = 0. \quad (24)$$

We recall that HPD and HND stand for Hermitian positive and negative definite matrix, respectively. From (15), (16) and the triangle inequality, it follows that $||\mathbb{W}_{\text{sca}}^\pm|| \leq ||T_e^\pm||^2 + ||T_m^\pm||^2$ and $||\mathbb{X}_{\text{sca}}^\pm|| \leq 2 ||T_e^\pm|| ||T_m^\pm||$. Based on the former relations we establish the **breaking of helicity annihilation** \mathcal{h}_a relative to the scattered energy:

$$\mathcal{h}_a = \max_{\pm} \left(\frac{||\mathbb{X}_{\text{sca}}^\pm||}{||\mathbb{W}_{\text{sca}}^\pm||} \right). \quad (25)$$

This novel quantity vanishes for linearly polarized scattered light, i.e. $\mathcal{h}_a = 0$, as then scattering annihilates all incident helicity. In contrast, the breaking of helicity annihilation is one for scattered light of well-defined helicity; however, it is independent of the incident helicity, which means $\mathcal{h}_a = 1$ if the scattered light has the same helicity as, or opposite to, the helicity as the incident light.

Further, we introduce the **helicity variation** $h_v \in [-1, 1]$ by the eigenvalues $\lambda_i^{\mathbb{X}_{\text{sca}}^\pm}$ of the chirality scattering matrix, namely, $\mathbb{X}_{\text{sca}}^\pm \mathbf{v}_i = \lambda_i^{\mathbb{X}_{\text{sca}}^\pm} \mathbf{v}_i$ as

$$h_v = \frac{1}{2} \left(\frac{\sum_i \lambda_i^{\mathbb{X}_{\text{sca}}^+}}{\sum_i |\lambda_i^{\mathbb{X}_{\text{sca}}^+}|} - \frac{\sum_i \lambda_i^{\mathbb{X}_{\text{sca}}^-}}{\sum_i |\lambda_i^{\mathbb{X}_{\text{sca}}^-}|} \right). \quad (26)$$

According to this definition, a helicity-keeping scatterer has $h_v > 0$, while a helicity-flipping one has $h_v < 0$. Note that a necessary condition for a scatterer to be anti-dual is to be perfectly helicity-flipping, i.e. $h_v = -1$. Conversely, for a dual scatterer the condition $h_v = 1$ (namely, to be perfectly helicity-keeping) is necessary. However, these two last conditions for h_v are not sufficient for either duality or anti-duality, and thus they may be regarded as weaker forms of these two latter properties.

Specifically, the helicity variation only takes the sign of the eigenvalues of \mathbb{X}_{sca} into account. For a dual scatterer not only the sign of the incident helicity has to be preserved, but the eigenvalues of \mathbb{X}_{sca} and \mathbb{W}_{sca} must be of equal absolute value. So, $h_v = 1$ is a weaker condition than $\mathcal{d} = 0$ since $h_v = 1$ means that the scattered light is dominated by the incident helicity, but it may not possess well-defined helicity. On the other hand, $\mathcal{d} = 0$ implies that the scattered light has well-defined helicity equal to that of the incident light.

As described above, perfectly helicity-keeping ($h_v = 1$) and perfectly helicity-flipping ($h_v = -1$) are weaker conditions of duality and anti-duality. These conditions may be further weakened yielding helicity-keeping ($h_v > 0$)

and helicity-flipping ($h_v < 0$) objects. Since the helicity variation (26) is a weighted average over all eigenvalues of \mathbb{X}_{sca} , h_v describes the mean alteration of the sign of the scattered chirality for all possible incident fields of well-defined helicity. For a helicity-keeping scatterer, the chirality scattering is dominated by incident fields for which the incident and the scattered helicity equal one-another. It does not imply that the helicity of all possible incident fields is unchanged, however, the major contribution to scattering is due to incident fields with preserved helicity. Accordingly, for strongly scattering illuminations of well-defined helicity, the scattered helicity changes sign predominantly for a helicity-flipping scatterer.

Chirality

Starting from (18), the chirality c and the g -factor of a scatterer are defined as

$$c = \overline{W_{\text{ext}}^+} - \overline{W_{\text{ext}}^-}, \quad g = \frac{\overline{W_{\text{ext}}^+} - \overline{W_{\text{ext}}^-}}{\overline{W_{\text{ext}}^+} + \overline{W_{\text{ext}}^-}}, \quad (27)$$

where the average bars should be understood as written in (18) and (19). Hence, these quantities represent the plane-wave averaged values derived from the full T -matrix, and are the corresponding generalizations for wide sense dipolar particles [20]. We notice that during the writing of this manuscript, a T -matrix formalism introducing quantities similar to those of Eq. (27) has been developed in Ref. [53].

Discussion of Examples

Isotropic Scatterer

Dipolar Isotropic Scatterer

Electromagnetic scattering by non-Rayleigh dipolar isotropic scattering objects is described by their electric and magnetic polarizabilities, α_e and α_m , and by their cross electric-magnetic ones, α_{em} and α_{me} . We assume reciprocal scatterers with $\alpha_{em} = -\alpha_{me}$. With a_1 , b_1 and c_1 being the electric, magnetic and cross electric-magnetic first Mie coefficients, it is well-known that $\alpha_e = \frac{6i\pi\epsilon_0}{k^3}a_1$, $\alpha_m = \frac{6i\pi\mu_0}{k^3}b_1$ and $\alpha_{me} = \frac{6i\pi\sqrt{\epsilon_0\mu_0}}{k^3}c_1$. In terms of these polarizabilities, one has for the quantities introduced above:

$$W_{\text{ext}}^{\pm} \propto \text{Im}(\alpha_e + \alpha_m) \pm 2 \text{Re}(\alpha_{em}), \quad (28)$$

$$W_{\text{sca}}^{\pm} \propto 2|\alpha_{em}|^2 \mp 2 \text{Im}(\alpha_{em}^* \{\alpha_e + \alpha_m\}) + |\alpha_e|^2 + |\alpha_m|^2, \quad (29)$$

$$X_{\text{sca}}^{\pm} \propto -2 \text{Im}(\alpha_{em}^* \{\alpha_e + \alpha_m\}) \pm 2 \text{Re}(\alpha_e^* \alpha_m) \pm 2|\alpha_{em}|^2, \quad (30)$$

$$\not{d} = \max_{\pm} \left(\frac{|\alpha_e - \alpha_m|}{|\alpha_e \pm \alpha_{em}| + |\alpha_m \pm \alpha_{em}|} \right), \quad (31)$$

$$\not{d} = \max_{\pm} \left(\frac{|\alpha_e + \alpha_m \pm 2\alpha_{em}|}{|\alpha_e \pm \alpha_{em}| + |\alpha_m \pm \alpha_{em}|} \right), \quad (32)$$

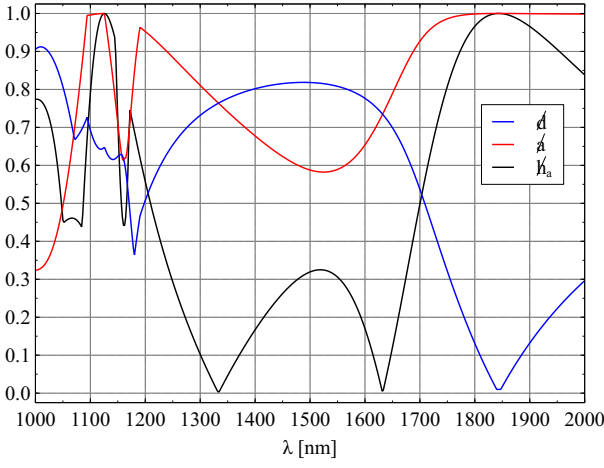
$$c \propto \text{Re}(\alpha_{em}), \quad (33)$$

$$g = \frac{2 \text{Re}(\alpha_{em})}{\text{Im}(\alpha_e + \alpha_m)}. \quad (34)$$

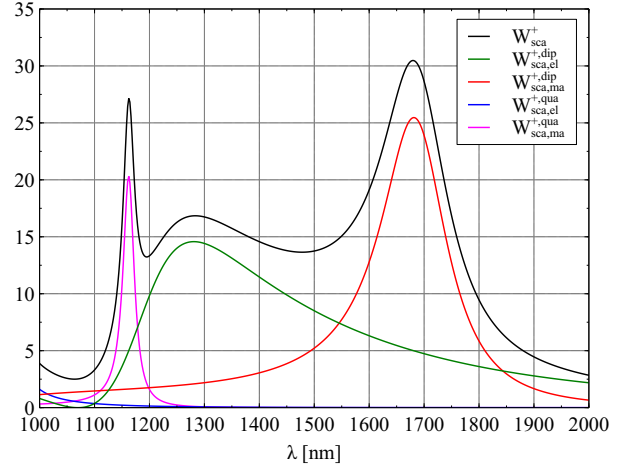
In general, the four experimental observables W_{ext}^{\pm} and W_{sca}^{\pm} are not sufficient to determine the real and imaginary parts of those three polarizabilities. Therefore, we propose the additional measurement of the scattered chirality X_{sca}^{\pm} . This together with Eqs. (28)-(34) should enable the full optical characterization of a dipolar scattering object.

The g -factor expressed by (27) is well-known: it is the dissymmetry factor [54, 45] of circular dichroism (see e.g. [20, cf. Eq. (6)]). Furthermore, the chirality (or helicity) c , being the differential extinction due to incident circularly polarized light, is proportional to the real part of the cross electric-magnetic polarizability α_{em} [20]. This measures the optical activity of the scatterer like e.g. a chiral nanoparticle or molecule [45].

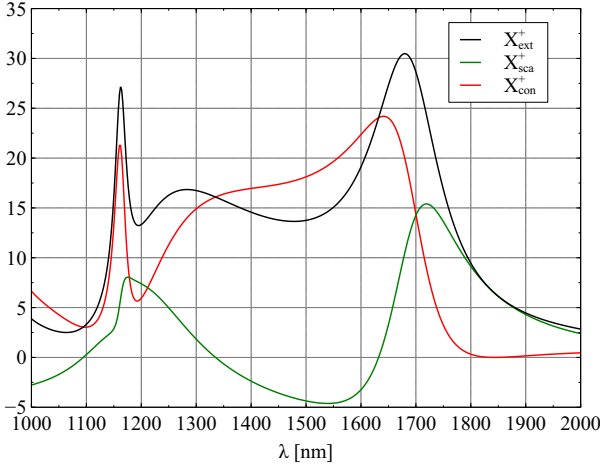
A dipolar body with $\alpha_e = \alpha_m$ (and as stated above, $\alpha_{em} = -\alpha_{me}$) guarantees duality symmetry [33]; thus it presents a vanishing duality breaking parameter ($\not{d} = 0$). This requirement coincides with the first Kerker condition [55, 56, 57, 58, 59, 60, 61, 62, 63, 64] according to which there is zero backscattered intensity under plane wave illumination. In fact, it has been shown that a dual scatterer produces zero-backscattering and that duality may be regarded as a generalization of the first Kerker condition [65]. On the other hand, the second Kerker condition [55] for achiral lossless objects ($\alpha_{em} = 0$) is $\text{Im}(\alpha_e) = \text{Im}(\alpha_m)$ and $\text{Re}(\alpha_e) = -\text{Re}(\alpha_m)$, yields a minimum of the forward scattered intensity [57] and also of the anti-duality breaking \not{d} . A scatterer with strictly vanishing \not{d} has been recognized as behaving as anti-dual [65]. Note that as a consequence of (32), a *chiral reciprocal non-Rayleigh dipolar particle, i.e. with $\alpha_{em} \neq 0$, cannot be anti-dual.*



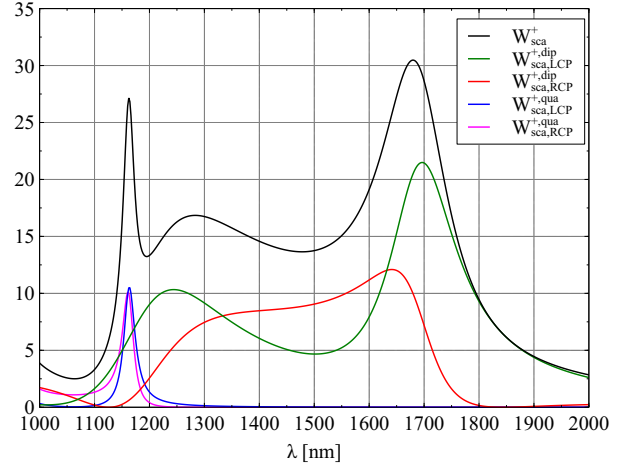
(a) classifying scalars



(b) electromagnetic multipolar W_{sca} [66, Fig. 3]



(c) chiral quantities



(d) W_{sca} in helicity basis

Figure 1: Spectra from a spherical Si particle of radius $r = 230\text{nm}$ and refractive index $n = 3.5$ illuminated by a left circularly polarized LCP (+) plane wave. (a) Breakings of duality \hat{d} , anti-duality \hat{d} and helicity annihilation \hat{h}_a . (b) Scattered energies due to the excitation of each of the induced electric and magnetic dipoles (at 1280nm and 1680nm, respectively), and magnetic quadrupole (at 1160nm), and total scattered energy due to the superposition of their respective scattered fields (after [66]). (c) Extinction, scattered, and conversion chiralities. (d) Multipolar scattered energies in the helicity basis (cf. main text). These are: due to the excitation of the RCP(-) dipole and quadrupole, $W_{\text{sca,RCP}}^{+, \text{dip}}$ (red line) and $W_{\text{sca,RCP}}^{+, \text{qua}}$ (pink line), respectively; as well as due to the excitation of the LCP(+) dipole and quadrupole, $W_{\text{sca,LCP}}^{+, \text{dip}}$ (green line) and $W_{\text{sca,LCP}}^{+, \text{qua}}$ (blue line), respectively. At dual behaviour ($\hat{d} = 0$), the chirality conversion X_{conv} vanishes, and anti-duality (minimal \hat{d}) is observed as a minimum in X_{sca} .

Achiral Isotropic Scatterer

Next, we first analyze the scattering by an achiral non-Rayleigh dipolar particle. Specifically, we address the behaviour of a spherical silicon (Si) nanoparticle of radius $r = 230\text{nm}$ and refractive index $n = 3.5$ in the near-infrared regime illuminated with a CPL plane wave of positive helicity, i.e. left circularly polarized, LCP(+). Since the sphere is an achiral scatterer, illumination with a CPL plane wave of negative helicity, i.e. right circularly polarized, RCP(-), yields equal results with regards to energy ($W_{\text{sca}}^- = W_{\text{sca}}^+$), while all chiral quantities present an additional minus sign (e.g. $X_{\text{sca}}^- = -X_{\text{sca}}^+$).

It has been shown that lossless dielectric particles of high permittivity, like this one, sustain strong magnetic dipoles and multipoles and hence are suitable constitutive elements for new photonic materials and devices [67, 66, 68, 63, 64]. As depicted in Fig. 1(b), the particle shows dipolar behaviour at incident wavelengths larger than 1200nm, exhibiting an electric and magnetic dipole peak at 1280nm and 1680nm, respectively [66, reproduced here as Fig. 1(b) to ease understanding].

Fig. 1(a) shows that the particle has $\hat{d} = 0$ only at the incident wavelength $\lambda \approx 1830\text{nm}$, where it is dual. Here, the first Kerker condition is fulfilled since the electric and magnetic total scattering cross-sections are equal [Fig. 1(b)] for the incident LCP(+) plane wave. Since the latter equivalence is necessary but not sufficient for zero-backscattering, the dual behaviour is more intuitively observed by noting that the incident polarization remains unchanged; i.e. the scattered field has the same helicity as the incident wave and, hence, the chirality conversion due to the scattering is zero, $X_{\text{conv}}^+ = 0$ [see Fig. 1(c)].

Concerning the second Kerker condition, manifested as a minimum of the differential scattering cross-section in the forward direction, here observed at $\lambda \approx 1550\text{nm}$ where, once again, the electric and magnetic parts of the scattered energy are equal [see Fig. 1(b)], the anti-duality breaking ϕ is at a local minimum of 0.59 [cf. Fig. 1(a)]. However, the breaking of helicity annihilation \mathcal{H}_a is at a local maximum. Note in this connection that a fully anti-dual scatterer yielding $\phi=0$, would give rise to $\mathcal{H}_a = 1$. Nevertheless, due to causality, a fully anti-dual behaviour is unphysical for lossless particles [57]. A perfect anti-dual scatterer would convert the incident circular polarization fully into its opposite handedness. Here, it should be stressed that the sign of the scattered chirality X_{sca}^+ (30) involves both amplitudes and phases of the polarizabilities. Accordingly, the scattered chirality is at a minimum for this wavelength of minimum forward scattering [cf. Fig. 1(c)].

Furthermore, depolarization effects such as Rayleigh depolarization at long wavelengths [69], are described by the breaking of helicity annihilation \mathcal{H}_a . In Fig. 1(a), it is observed that at both $\lambda \approx 1330\text{nm}$ and $\lambda \approx 1640\text{nm}$ the scattered light is achiral, i.e. linearly polarized. This property is observable as a vanishing scattered chirality $X_{\text{sca}} = 0$ [Fig. 1(c)]. At these wavelengths, the contributions of the particle induced dipoles, yielding positive and negative helicity in the scattered energy, are equal and thus cancel each other [Fig. 1(d)]. As a result, an achiral response of the isotropic dipolar scatterer takes place.

The interplay between the electric and magnetic induced multipoles in these magnetodielectric particles gives rise to excitations in the body whose helicity is either the same or opposite to that of the incident wave; namely, dipoles and multipoles induced in the sphere, that represented in the helicity basis [cf. (14)] are of positive [LCP(+)] or negative [RCP(-)] helicity. Both kinds of excitations appear in the case of incident LCP(+) plane wave illumination. For example, a LCP(+) dipole is due to an electric dipole \mathbf{d} which oscillates with a positive phase shift of π with respect to a magnetic dipole \mathbf{m} of equal amplitude ($\mathbf{d} = i\mathbf{m}/c$) [48, 70]. Conversely, a negative helicity RCP(-) electric dipole has a phase shift of $-\pi$ compared to the corresponding magnetic dipole, i.e. $\mathbf{d} = -i\mathbf{m}/c$. Thus we denote their positive and negative helicity property with *subscripts* LCP and RCP, respectively. In general, both kind of dipoles are induced by an incident wave of given helicity, and they determine the polarization of the *scattered* field. We recall that as introduced before, the *superscripts* \pm stand for *incident* light of positive and negative helicity, respectively.

The dipoles and multipoles of helicity opposite to that of the incident wave are associated to the conversion of chirality (or helicity) on scattering. This phenomenon is seen when we compare this chirality conversion X_{conv}^+ [cf. red line in Fig. 1(c)] and the excitation of induced dipoles and quadrupoles, which expressed in the helicity basis have negative handedness, [see $W_{\text{sca,RCP}}^{+, \text{dip}}$ and $W_{\text{sca,RCP}}^{+, \text{qua}}$, red and pink lines, respectively, in Fig. 1(d)]. On the basis of the criterion above, these two latter excitations have helicity [RCP (-)] opposite to that of the incident wave which has been chosen as positive [LCP (+)], as explained before.

Hence, taking into account that the scatterer is lossless and that, as just seen, the scattered energy consists of two parts: one of negative and one of positive helicity, it follows that the total scattered energy W_{ext}^+ due to this incident plane wave with positive helicity LCP(+) is written as: $W_{\text{ext}}^+ = W_{\text{sca}}^+ = W_{\text{sca,LCP}}^+ + W_{\text{sca,RCP}}^+$. Furthermore, the scattered chirality measures the difference of these two contributions [71]: $X_{\text{sca}}^+ \propto W_{\text{sca,LCP}}^+ - W_{\text{sca,RCP}}^+$. From the equivalence of extinction of both energy and chirality for incident fields of well-defined helicity [cf. (17)], we deduce that *for a lossless scatterer the chirality conversion is given by twice the scattered energy of opposite helicity*, i.e. $X_{\text{conv}}^+ \propto 2W_{\text{sca,RCP}}^+$. This is confirmed in the dipolar regime ($\lambda > 1200\text{nm}$), as well as around 1170nm where the magnetic quadrupole dominates; and shows the significance of this novel observable, namely the chirality conversion, specifically for scattering objects that, like these high refractive index dielectric particles, exhibit a strong magnetic response to the incident field.

Chiral Isotropic Scatterer

Now, we introduce chirality in the geometrically isotropic scatterer by means of a non-zero chirality parameter κ , while this body remains reciprocal and bi-isotropic [46]. For lossless media, the absolute value of κ is smaller than unity [46, Eq. (D.8)], as stated above. Here, as before, we fix the sphere radius $r = 230\text{nm}$ and its refractive index $n = 3.5$. The chirality parameter κ is then varied from zero (which would be the case discussed above) to unity. Of course now the particle will no longer be made of Si, since $\kappa \neq 0$ makes the material hypothetical. Nevertheless, this yields a direct way of studying the interplay of significant magnetodielectric effects with phenomena stemming from the chirality of the scattering object.

The breakings of duality and helicity annihilation, as well as the helicity variation, are shown in Fig. 2(a)-(c). These quantities are symmetric with respect to $\kappa = 0$, while the g -factor is antisymmetric [Fig. 2(d)]. For vanishing κ , the scatterer is achiral and, accordingly, $g = 0$. The magnetic quadrupole resonance at 1160nm of the achiral particle is clearly red-shifted and yields very large g -factors up to one. Interestingly, the sign of g is not directly coupled to the sign of the chirality parameter, but changes over the analyzed spectrum: regions of highly positive, as well as of very negative, g -factor occur throughout this parameter domain. In this regard, it should be noted that natural materials usually possess very small effective chirality parameters [72], these being in the range of 10^{-3} .

A very unusual behaviour is observed in the duality of this magnetodielectric object with high κ [Fig. 2(a)]: at $\kappa \approx 0.85$, the scatterer is dual irrespective of the incident wavelength. Due to the red-shifted interference of magnetic quadrupole and electric dipole resonances, the particle is even stably dual with respect to both λ and κ in this regime. This stable minimum in ϕ is visible as a cross-like structure centered at $\lambda \approx 1250\text{nm}$ and $\kappa \approx 0.85$. Although in the range of wavelengths in this study, the particle shows either dipolar or quadrupolar behaviour depending on λ ,

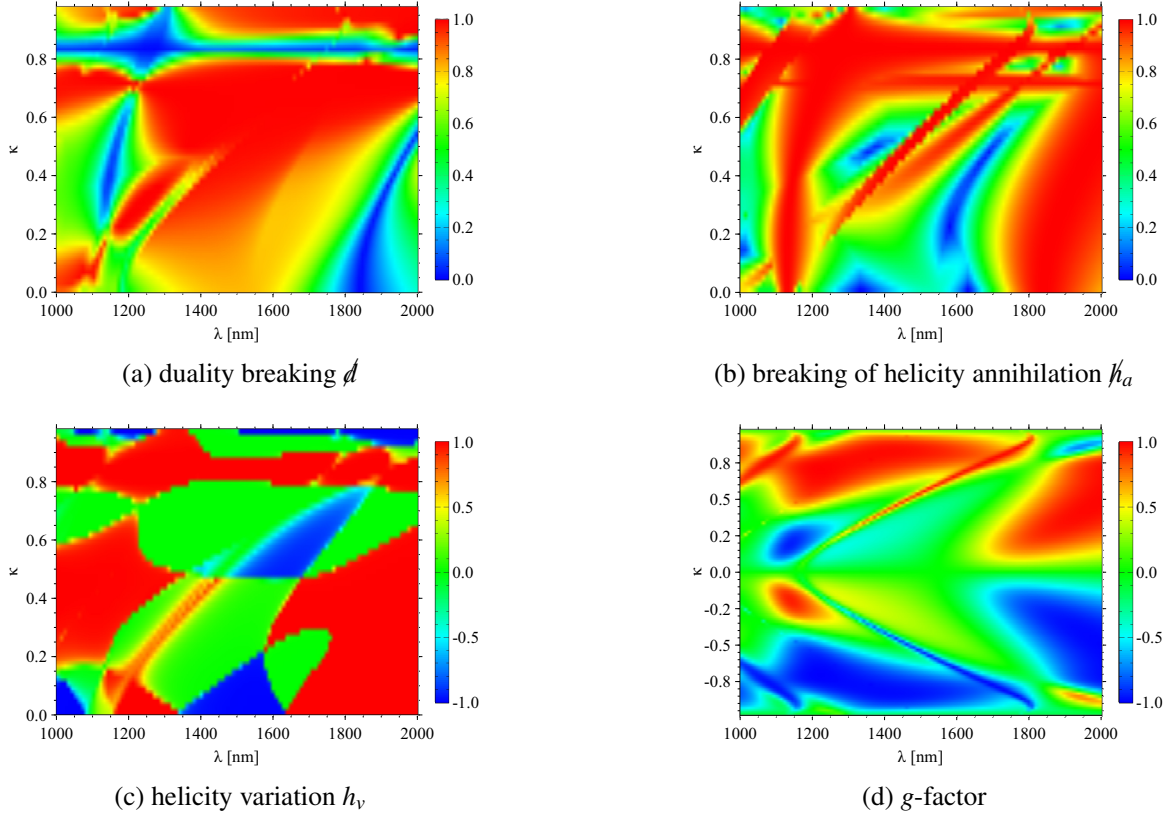


Figure 2: Spherical chiral particle of radius $r = 230\text{nm}$, refractive index $n = 3.5$ and varying chirality parameter $\kappa \neq 0$. Colorbars indicate breakings of: (a) duality \bar{d} and (b) helicity annihilation \bar{h}_a ; as well as (c) helicity variation h_v and (d) the g -factor. The wavelength at which the achiral particle ($\kappa = 0$) behaves as dual is red-shifted, and for a large κ the particle is dual independently of the wavelength. The long wavelength achiral helicity annihilation is also red-shifted, whereas the short wavelength achiral peak is vanishing for increasing chirality. The helicity variation resembles the qualitative behaviour of duality. The quantities \bar{d} , \bar{h}_a and h_v are symmetric with respect to κ ; while the g -factor changes sign for positive and negative κ , and, being strongly wavelength dependent, it generally increases as so does $|\kappa|$.

the stability of its dual behaviour is more intuitively understood in the dipolar domain. For $\kappa > 0.85$, the electric polarizability is dominant, whereas for chirality parameters smaller than 0.85, the magnetic response is larger (not shown for the sake of brevity). The change from a predominantly electric response to a magnetic one occurs at $\kappa = 0.85$ throughout the spectrum. Here, the first Kerker condition $\alpha_e = \alpha_m$ yields vanishing duality breaking [cf. Eq.(31)] with cross electric-magnetic polarizabilities α_{em} of an order similar to that of the electric and magnetic ones. Additionally, the achiral dual resonance at 1830nm is again red-shifted.

This overall red-shift is also apparent in the breaking of helicity annihilation [Fig. 2(b)]. The first helicity annihilation resonance at $\lambda \approx 1330\text{nm}$ vanishes as the chirality parameter shows up because the red-shifted magnetic quadrupole peak is then larger and exhibits a non-zero scattered helicity. Concerning the annihilation peak at 1640nm in the achiral case [cf. Fig. 1(a)], it is stable up to $\kappa \approx 0.6$. For larger chirality parameters, the resonance of helicity annihilation vanishes and barely there are regimes of similar behaviour, i.e. most scattered light is not linearly polarized for incident fields of well-defined helicity. The general trends of both duality and helicity annihilation breakings are also visible in the helicity variation, however, since this condition is weaker for both dual and helicity annihilating behaviour, as discussed before, the areas of extreme h_v -values are better distinguishable with sharp transitions from positive to negative h_v [Fig. 2(c)].

Anisotropic Scatterer

The study of non-spherical anisotropic scatterers is highly dependent on the direction of illumination. Chiral molecules are often analyzed in dilute solutions wherein they are randomly oriented. Mostly, only small numbers of single molecules are available and multiple scattering can be neglected. The quantities introduced above are suitable for the analysis of such isolated scatterers, as we show in the next two illustrations: (iii) and (iv).

We wish to remark that in recent experiments, the helicity components of the scattered light were measured in transmission [73] and discussed by dual symmetry [74]. Furthermore, a chirality flux spectroscopy, measuring the third Stokes parameter, was used to analyze the chiroptical response of two-dimensional chiral structures [75]. We note that the helicity of light has been measured mostly in transmission. By contrast, our study addresses the importance of the full angular averaged chirality flux. This quantity may be measured in an integrating sphere, or by combining

measurements in forward and backward directions as in Ref. [70].

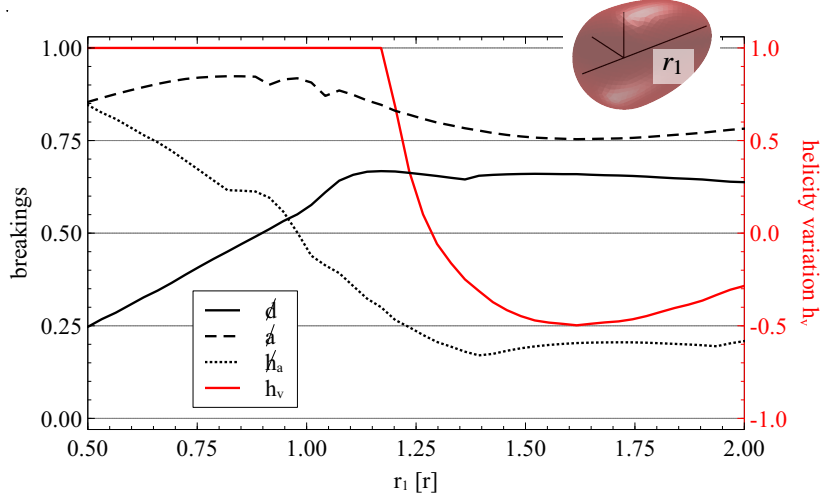


Figure 3: Convex body with shrunk ($\frac{r_1}{r} < 1$) and elongated ($\frac{r_1}{r} > 1$) radius r_1 in one direction starting from a sphere with $r = 230\text{nm}$ (cf. main text). The incident wavelength is 1680nm and the electric permittivity $\varepsilon = \sqrt{3.5}$. The breakings of duality d , anti-duality a and helicity annihilation h_a , as well as the helicity variation h_v are displayed. Prolated shapes are helicity-keeping and approach dual behaviour. The dominating sign of the scattered chirality is flipped with respect to that of the incident light ($h_v < 0$) for $\frac{r_1}{r} > 1.3$. However, this scattered light is depolarized with a breaking of helicity annihilation of approximately 0.2.

Achiral Anisotropic Scatterer

Next, we first numerically study the scattering from a convex body with the help of the Finite Element Method (cf. section Methods). The six different radii of a generalized ellipsoid are fixed except the one: r_1 . Again, we start from the magnetodielectric sphere with $r = 230\text{nm}$ and refractive index $n = 3.5$. As this object is transformed into an ellipsoid, the varying radius r_1 is shrunk ($\frac{r_1}{r} < 1$) to its half and stretched ($\frac{r_1}{r} > 1$) to its double value. For simplicity, we fix the incident wavelength to 1680nm , which, as seen above, coincides with the resonance peak of the magnetic dipole when this object is spherical.

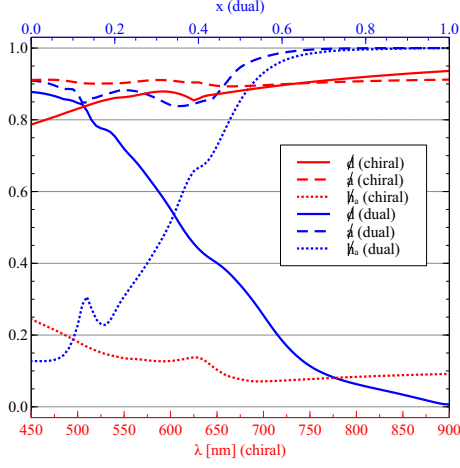
Since there exist at least two mirror-planes in this geometrically achiral body, both the chirality and g -factor vanish. As shown in Fig. 3, the scatterer is perfectly helicity-keeping with $h_v = 1$ for $\frac{r_1}{r} < 1.2$. The duality breaking decreases for prolate shapes with a minimal value of 0.2 at half the initial sphere radius. Above $\frac{r_1}{r} = 1.2$, the duality breaking remains nearly constant, but the helicity variation reveals that the incident helicity sign changes in the scattered field for $\frac{r_1}{r} > 1.3$. However, the object is not anti-dual in the strict sense, since the anti-duality breaking is larger than 0.8 in the full parameter space, and only the dominating sign of the eigenvalues of the scattered chirality is represented in the helicity variation. Furthermore, there is no helicity annihilation at this wavelength and geometric variations. The minimal value of the breaking of helicity annihilation is approximately 0.2 for elongated shapes.

Chiral Dual Anisotropic Scatterer

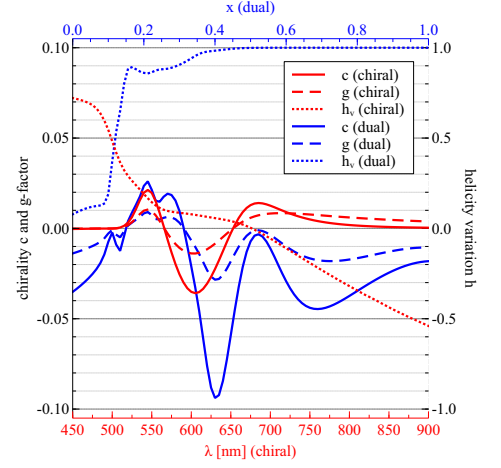
In what follows we illustrate our formalism for chiral anisotropic particles. We start by analyzing their duality breaking. A chiral gold particle resulting from a sophisticated fabrication procedure, and studied experimentally [41], is made dual by introducing a magnetic permeability. Namely, the particle is analyzed for an incident wavelength of 600nm , the permittivity ε is kept constant at its value for gold at 600nm , while the permeability varies as $\mu = x(\varepsilon - 1) + 1$. The parameter x is a parameter that grows between 0 and 1, so that when $x = 1$, the particle is dual since $\varepsilon = \mu$ and thus $\alpha_e = \alpha_m$ [55].

As shown in Fig. 4(a) (blue lines), the duality breaking accurately depicts both the non-dual and dual behaviour of the particle as x varies from zero up to one ($d = 0$). The helicity variation with $h_v = 1$ is, as discussed before, a weaker condition for duality. The scatterer is already perfectly helicity-keeping for x larger than 0.5 [see Fig. 4(b)]. From this value of x on, more detailed information is contained in d . However, we can deduce from the spectrum of helicity variation that the scattered field is dominantly positive chiral for all artificial materials analyzed in this example, since $h_v > 0$ for all x . Furthermore, the anti-duality and helicity annihilation breakings are unity for $x > 0.7$, as expected for dual symmetric materials.

The chirality c and the g -factor reveal the highly chiral response of the particle. Large magnitudes of g -factors up to 0.1 are reached [see Fig. 4(b)]. This is partly attributed to the high scattering due to the very large refractive index $n \approx -10.14 + 1.38i$. Nevertheless, record g -factors with values up to 0.02 are also attained when the particle is purely made of gold. This g derived from the full T -matrix [cf. Eq. (27)] can be interpreted as the average differential



(a) breaking scalars



(b) chiral scalars

Figure 4: Geometrically chiral pyramidal particle made from gold [41] (upper inset and red lines) or from a dual material obtained by introducing a magnetic permeability at $\lambda = 600\text{nm}$ (lower inset and blue lines). (a) Breakings of duality \mathcal{d} , anti-duality \mathcal{d} and helicity annihilation \mathcal{h}_a dependent both on the wavelength for the gold particle and on the duality parameter $x \in [0, 1]$ for the dual particle, respectively. (b) Chirality c , g -factor (left axis), and helicity variation h (right axis). The gold particle is neither dual ($\mathcal{d} \neq 0$) nor anti-dual ($\mathcal{d} \neq 0$) but scatters mostly achiral light since $\mathcal{h}_a \approx 0.15$ over the whole spectrum. Its optically chiral response has been measured experimentally [41] and fits the simulated data. The dual particle illustrates the simultaneous conditions $\mathcal{d} = 0, \mathcal{d} = 1$ and $h = 1$ for a dual symmetric scatterer. Throughout the transition from gold ($x = 0$) to a dual particle ($x = 1$), the particle is dominantly negative chiral. The increase of the magnitude of chirality by a factor of six is partly due to the higher refractive index.

response due to incident right and left circularly polarized plane waves. Our simulated data of c and g correspond well with the experimentally measured results [41, cf. Figs. 3(b),(d)].

Chiral Anisotropic Scatterer

The helicity variation for the chiral gold particle shows a monotonic decreasing behaviour with a sign change at 680nm . For smaller wavelengths the scattered chirality flux mostly has positive helicity, whereas in the longer wavelength regime a negative helicity is observed. This yields near-fields which are dominated by positive and negative optical chirality hot-spots, respectively. Note, however, that this is only the case for the scattered field. The coupling of chiral molecules in the near-field is due to the total field composed of the incident and the scattered one [20]. Accordingly, interference effects might result in helicity-flipping fields for small wavelengths, even though $h_v > 0$. Nevertheless, the study of the helicity variation provides further insight than the study of the previously introduced breakings such as \mathcal{d} in this example. The breakings are constant over the spectrum of incident wavelengths and are not suitable for classifying the scattering response with respect to polarization phenomena, [see Fig. 4(a), red lines].

In conclusion, we have put forward the quantities derived from the conservation of optical chirality (or helicity) of monochromatic wavefields, both in Mie and T -matrix theories. Such quantities are scalars that characterize the response of arbitrary scattering particles. In particular, the breaking of dual symmetry is accompanied by a weaker condition based on the scattered chirality, namely, the so-called helicity variation.

Directional effects of the differential scattering cross-section, such as the Kerker conditions, have been included in this general formalism, both for achiral and chiral magnetodielectric dipolar spherical particles, and discussed with respect to the experimentally accessible data of scattered and extinguished energy and chirality. This has been illustrated with high permittivity, non-Rayleigh, dipolar spheres, which have generated so much interest in nanophotonics. We have shown how their illumination with chiral light uncovers new important phenomena associated to their chiral dipolar and quadrupolar resonant excitations, either with the same or with opposite helicity with respect to that of the illuminating wave.

Anisotropic scatterers, either with or without a mirror-plane, are classified by these novel quantities, and the implications for the scattered fields are discussed. As an illustration, a comparison with experimental data from a chiral gold particle has been drawn. We expect that this general framework enables the characterization of a broad range of scattering objects with applications in chiral molecular spectroscopy, spin photonics, and the design of optical sources as well as of metamaterials and other composite media.

Methods

Isotropic Mie Code

As described in the main text, the submatrices of the T -matrix of a geometrically isotropic scatterer are diagonal. The coefficients are given by [45, p. 188, adopted to non-even/-odd basis \mathbf{M}, \mathbf{N}]

$$\alpha_n = \frac{V_n(m_R)A_n(m_L) + V_n(m_L)A_n(m_R)}{W_n(m_L)V_n(m_R) + V_n(m_L)W_n(m_R)} \quad (35)$$

$$\beta_n = \frac{W_n(m_L)B_n(m_R) + W_n(m_R)B_n(m_L)}{W_n(m_L)V_n(m_R) + V_n(m_L)W_n(m_R)} \quad (36)$$

$$\gamma_n = \frac{W_n(m_R)A_n(m_L) - W_n(m_L)A_n(m_R)}{W_n(m_L)V_n(m_R) + V_n(m_L)W_n(m_R)}. \quad (37)$$

The coefficients α_n, β_n and γ_n are the main diagonal elements of T_{ee}, T_{mm} and T_{em} , respectively. The relative refractive indices m_L and m_R and the mean refractive index m are then defined as $m_L = \frac{n_L}{n_s}, m_R = \frac{n_R}{n_s}$ and $\frac{1}{m} = \frac{1}{2} \left(\frac{1}{m_R} + \frac{1}{m_L} \right) \frac{\mu}{\mu_s}$, where n_s and μ_s are the refractive index and the relative permeability of the surrounding medium, respectively. The results in Fig. 1 and 2 are obtained using these analytic solutions of Maxwell's equations.

Anisotropic Numerical Simulations

The solution of time-harmonic Maxwell's equations for arbitrary geometries are obtained with the commercial solver *JCMsuite* based on the Finite Element Method (FEM). The particles analyzed in Fig. 3 and 4 are discretized by tetrahedral meshes. Convergence is ensured for sidelength constraints of $h = 50\text{nm}$ and ansatz functions of polynomial degrees $p = 3$ and $p = 4$ for Fig. 3 and 4, respectively. The open boundary conditions are modelled by Perfectly Matched Layers which are controlled by a software-specific precision parameter[76] of $1e - 5$.

The T -matrices are computed by illumination with 36 and 88 plane waves, respectively. These are equally distributed on a sphere in k -space, and are created with random polarizations. This procedure yields accurate results up to multipoles of order $m = 3$ for the achiral ellipsoid and $m = 5$ for the chiral particle, respectively. The entries of the T -matrix are efficiently calculated by a surface integral based on the conservation of extinction [77].

References

- [1] Andrews, D. L. & Babiker, M. *The angular momentum of light* (Cambridge University Press, 2012).
- [2] Allen, L., Barnett, S. M. & Padgett, M. J. *Optical angular momentum* (CRC Press, 2003).
- [3] Allen, L., Padgett, M. & Babiker, M. The orbital angular momentum of light. In Wolf, E. (ed.) *Prog. Opt.*, vol. 39, 291–372 (Elsevier, 1999).
- [4] Schäferling, M., Dregely, D., Hentschel, M. & Giessen, H. Tailoring enhanced optical chirality: design principles for chiral plasmonic nanostructures. *Phys. Rev. X* **2**, 031010 (2012).
- [5] Schellman, J. A. Circular dichroism and optical rotation. *Chem. Rev.* **75**, 323–331 (1975).
- [6] Richardson, F. S. & Riehl, J. P. Circularly polarized luminescence spectroscopy. *Chem. Rev.* **77**, 773–792 (1977).
- [7] Vuong, L., Adam, A., Brok, J., Planken, P. & Urbach, H. Electromagnetic spin-orbit interactions via scattering of subwavelength apertures. *Phys. Rev. Lett.* **104**, 083903 (2010).
- [8] Bliokh, K. Y., Rodríguez-Fortuño, F., Nori, F. & Zayats, A. V. Spin-orbit interactions of light. *Nat. Photonics* **9**, 796 (2015).
- [9] Sukhov, S., Kajorndejnukul, V., Naraghi, R. R. & Dogariu, A. Dynamic consequences of optical spin-orbit interaction. *Nat. Photonics* **9**, 809 (2015).
- [10] Hakobyan, D. & Brasselet, E. Optical torque reversal and spin-orbit rotational doppler shift experiments. *Opt. Express* **23**, 31230–31239 (2015).
- [11] Hosten, O. & Kwiat, P. Observation of the spin hall effect of light via weak measurements. *Science* **319**, 787–790 (2008).
- [12] Bliokh, K. Y., Smirnova, D. & Nori, F. Quantum spin hall effect of light. *Science* **348**, 1448–1451 (2015).
- [13] Andrews, D. L., Coles, M. M., Williams, M. D. & Bradshaw, D. S. Expanded horizons for generating and exploring optical angular momentum in vortex structures. In *Proc. SPIE*, vol. 8813, 88130Y (2013).

- [14] OSullivan, M. N., Mirhosseini, M., Malik, M. & Boyd, R. W. Near-perfect sorting of orbital angular momentum and angular position states of light. *Opt. Express* **20**, 24444–24449 (2012).
- [15] Krenn, M., Tischler, N. & Zeilinger, A. On small beams with large topological charge. *New J. Phys.* **18**, 033012 (2016).
- [16] Bradshaw, D. S., Leeder, J. M., Coles, M. M. & Andrews, D. L. Signatures of material and optical chirality: Origins and measures. *Chem. Phys. Lett.* **626**, 106–110 (2015).
- [17] Nieto-Vesperinas, M. Non-zero helicity extinction in light scattered from achiral (or chiral) small particles located at points of null incident helicity density. *J. Opt.* **19**, 065402 (2017).
- [18] Bliokh, K. Y., Kivshar, Y. S. & Nori, F. Magnetoelectric effects in local light-matter interactions. *Phys. Rev. Lett.* **113**, 033601 (2014).
- [19] Vincent, R. & Carminati, R. Magneto-optical control of Förster energy transfer. *Phys. Rev. B* **83**, 165426 (2011).
- [20] Tang, Y. & Cohen, A. E. Optical chirality and its interaction with matter. *Phys. Rev. Lett.* **104**, 163901 (2010).
- [21] Tang, Y. & Cohen, A. E. Enhanced enantioselectivity in excitation of chiral molecules by superchiral light. *Science* **332**, 333–336 (2011).
- [22] Guzatov, D. V. & Klimov, V. V. The influence of chiral spherical particles on the radiation of optically active molecules. *New J. Phys.* **14**, 123009 (2012).
- [23] Alaeian, H. & Dionne, J. A. Controlling electric, magnetic, and chiral dipolar emission with pt-symmetric potentials. *Phys. Rev. B* **91**, 245108 (2015).
- [24] Hentschel, M., Schäferling, M., Duan, X., Giessen, H. & Liu, N. Chiral plasmonics. *Sci. Adv.* **3**, e1602735 (2017).
- [25] Kramer, C., Schäferling, M., Weiss, T., Giessen, H. & Brixner, T. Analytic optimization of near-field optical chirality enhancement. *ACS Photonics* **4**, 396–406 (2017).
- [26] García-Etxarri, A. & Dionne, J. A. Surface-enhanced circular dichroism spectroscopy mediated by nonchiral nanoantennas. *Phys. Rev. B* **87**, 235409 (2013).
- [27] Wang, H., Li, Z., Zhang, H., Wang, P. & Wen, S. Giant local circular dichroism within an asymmetric plasmonic nanoparticle trimer. *Sci. Rep.* **5**, 8207 (2015).
- [28] Lv, T. *et al.* Hybrid metamaterial switching for manipulating chirality based on vo 2 phase transition. *Sci. Rep.* **6**, 23186 (2016).
- [29] Hu, L., Tian, X., Huang, Y., Fang, L. & Fang, Y. Quantitatively analyzing the mechanism of giant circular dichroism in extrinsic plasmonic chiral nanostructures by tracking the interplay of electric and magnetic dipoles. *Nanoscale* **8**, 3720–3728 (2016).
- [30] Lipkin, D. M. Existence of a new conservation law in electromagnetic theory. *J. Math. Phys.* **5**, 696–700 (1964).
- [31] Bliokh, K. Y. & Nori, F. Characterizing optical chirality. *Phys. Rev. A* **83**, 021803 (2011).
- [32] Cameron, R. P., Barnett, S. M. & Yao, A. M. Optical helicity, optical spin and related quantities in electromagnetic theory. *New J. Phys.* **14**, 053050 (2012).
- [33] Nieto-Vesperinas, M. Optical theorem for the conservation of electromagnetic helicity: Significance for molecular energy transfer and enantiomeric discrimination by circular dichroism. *Phys. Rev. A* **92**, 023813 (2015).
- [34] Nieto-Vesperinas, M. Chiral optical fields: a unified formulation of helicity scattered from particles and dichroism enhancement. *Phil. Trans. R. Soc. A* **375**, 20160314 (2017).
- [35] Gutsche, P., Schneider, P.-I., Burger, S. & Nieto-Vesperinas, M. Chiral scatterers designed by bayesian optimization. In *International Workshop on Metamaterials-by-Design, IOP Conf. Series: Journal of Physics* **963**, 012004 (2018). arXiv:1712.07091.
- [36] Gutsche, P., Poulikakos, L. V., Hammerschmidt, M., Burger, S. & Schmidt, F. Time-harmonic optical chirality in inhomogeneous space. In *Proc. SPIE 9756*, 97560X (2016). arXiv:1603.05011.
- [37] Poulikakos, L. V. *et al.* Optical chirality flux as a useful far-field probe of chiral near fields. *ACS Photonics* **3**, 1619–1625 (2016).
- [38] Mishchenko, M., Travis, L. & Lacis, A. *Scattering, Absorption, and Emission of Light by Small Particles* (Cambridge University Press, 2002).

- [39] Le Ru, E. C., Somerville, W. R. & Auguie, B. Radiative correction in approximate treatments of electromagnetic scattering by point and body scatterers. *Phys. Rev. A* **87**, 012504 (2013).
- [40] Fernandez-Corbaton, I. *Helicity and duality symmetry in light matter interactions: Theory and applications*. Ph.D. thesis, Macquarie University, Department of Physics and Astronomy (2014).
- [41] McPeak, K. M. *et al.* Complex chiral colloids and surfaces via high-index off-cut silicon. *Nano Lett.* **14**, 2934–2940 (2014).
- [42] Jackson, J. D. *Classical Electrodynamics* (John Wiley and Sons, 1998), 3rd edn.
- [43] Nieto-Vesperinas, M. *Scattering and diffraction in physical optics* (World Scientific Publishing Company, 2006), 2nd edn.
- [44] Waterman, P. C. Matrix formulation of bistatic electromagnetic scattering. Tech. Rep., MITRE CORP BED-FORD MA (1968).
- [45] Bohren, C. F. & Huffman, D. R. *Absorption and Scattering of Light by Small Particles* (John Wiley & Sons, 1940).
- [46] Lindell, I. V. & Sihvola, A. H. *Electromagnetic wave in chiral and bi-isotropic media* (Artech House, 1994).
- [47] Fruhnert, M., Fernandez-Corbaton, I., Yannopapas, V. & Rockstuhl, C. Computing the T-matrix of a scattering object with multiple plane wave illuminations. *Beilstein J. Nanotechnol.* **8**, 614–626 (2017).
- [48] Fernandez-Corbaton, I. & Molina-Terriza, G. Role of duality symmetry in transformation optics. *Phys. Rev. B* **88**, 085111 (2013).
- [49] Zambrana-Puyalto, X. & Bonod, N. Tailoring the chirality of light emission with spherical si-based antennas. *Nanoscale* **8**, 10441–10452 (2016).
- [50] Fernandez-Corbaton, I., Rockstuhl, C. & Klopper, W. Computation of electromagnetic properties of molecular ensembles. *arXiv preprint arXiv:1804.08085* (2018).
- [51] Fernandez-Corbaton, I., Fruhnert, M. & Rockstuhl, C. Objects of maximum electromagnetic chirality. *Phys. Rev. X* **6**, 031013 (2016).
- [52] Fernandez-Corbaton, I., Fruhnert, M. & Rockstuhl, C. Dual and chiral objects for optical activity in general scattering directions. *ACS Photonics* **2**, 376–384 (2015).
- [53] Suryadharma, R. N. & Rockstuhl, C. Predicting Observable Quantities of Self-Assembled Metamaterials from the T-Matrix of Its Constituting Meta-Atom. *Materials* **11**, 213 (2018).
- [54] Craig, D. P. & Thirunamachandran, T. *Molecular quantum electrodynamics: an introduction to radiation-molecule interactions* (Courier Corporation, 1984).
- [55] Kerker, M., Wang, D.-S. & Giles, C. Electromagnetic scattering by magnetic spheres. *J. Opt. Soc. Am.* **73**, 765–767 (1983).
- [56] Gomez-Medina, R. *et al.* Electric and magnetic dipolar response of germanium nanospheres: interference effects, scattering anisotropy, and optical forces. *J. Nanophotonics* **5**, 053512 (2011).
- [57] Nieto-Vesperinas, M., Gomez-Medina, R. & Saenz, J. Angle-suppressed scattering and optical forces on submicrometer dielectric particles. *J. Opt. Soc. Am. A* **28**, 54–60 (2011).
- [58] Geffrin, J.-M. *et al.* Magnetic and electric coherence in forward-and back-scattered electromagnetic waves by a single dielectric subwavelength sphere. *Nat. Commun.* **3**, 1171 (2012).
- [59] Fu, Y. H., Kuznetsov, A. I., Miroshnichenko, A. E., Yu, Y. F. & Lukyanchuk, B. Directional visible light scattering by silicon nanoparticles. *Nat. Commun.* **4**, 1527 (2013).
- [60] Person, S. *et al.* Demonstration of zero optical backscattering from single nanoparticles. *Nano Lett.* **13**, 1806–1809 (2013).
- [61] Staude, I. *et al.* Tailoring directional scattering through magnetic and electric resonances in subwavelength silicon nanodisks. *ACS Nano* **7**, 7824–7832 (2013).
- [62] Zhang, Y., Nieto-Vesperinas, M. & Sáenz, J. J. Dielectric spheres with maximum forward scattering and zero backscattering: a search for their material composition. *J. Opt.* **17**, 105612 (2015).
- [63] Decker, M. & Staude, I. Resonant dielectric nanostructures: a low-loss platform for functional nanophotonics. *J. Opt.* **18**, 103001 (2016).

- [64] Kuznetsov, A. I., Miroshnichenko, A. E., Brongersma, M. L., Kivshar, Y. S. & Lukyanchuk, B. Optically resonant dielectric nanostructures. *Science* **354**, aag2472 (2016).
- [65] Zambrana-Puyalto, X., Fernandez-Corbaton, I., Juan, M., Vidal, X. & Molina-Terriza, G. Duality symmetry and kerker conditions. *Opt. Lett.* **38**, 1857–1859 (2013).
- [66] García-Etxarri, A. *et al.* Strong magnetic response of submicron silicon particles in the infrared. *Opt. Express* **19**, 4815–4826 (2011). arXiv:1005.5446.
- [67] Evlyukhin, A. B., Reinhardt, C., Seidel, A., Lukyanchuk, B. S. & Chichkov, B. N. Optical response features of Si-nanoparticle arrays. *Phys. Rev. B* **82**, 045404 (2010).
- [68] Kuznetsov, A. I., Miroshnichenko, A. E., Fu, Y. H., Zhang, J. & Lukyanchuk, B. Magnetic light. *Sci. Rep.* **2**, 492 (2012).
- [69] van der Laan, J. D., Wright, J. B., Scrymgeour, D. A., Kemme, S. A. & Dereniak, E. L. Evolution of circular and linear polarization in scattering environments. *Opt. Express* **23**, 31874–31888 (2015).
- [70] Wozniak, P. *et al.* Chiroptical response of a single plasmonic nanohelix. *arXiv preprint arXiv:1804.05641* (2018).
- [71] Gutsche, P., Mäusle, R. & Burger, S. Locally enhanced and tunable optical chirality in helical metamaterials. *Photonics* **3**, 60 (2016).
- [72] Schäferling, M., Engheta, N., Giessen, H. & Weiss, T. Reducing the complexity: Enantioselective chiral near-fields by diagonal slit and mirror configuration. *ACS Photonics* **3**, 1076–1084 (2016).
- [73] Tischler, N. *et al.* Experimental control of optical helicity in nanophotonics. *Light: Science & Applications* **3**, e183 (2014).
- [74] Fernandez-Corbaton, I. *et al.* Electromagnetic duality symmetry and helicity conservation for the macroscopic maxwells equations. *Physical review letters* **111**, 060401 (2013).
- [75] Poulidakos, L. V., Thureja, P., Stollmann, A., De Leo, E. & Norris, D. J. Chiral light design and detection inspired by optical antenna theory. *Nano Lett.* (2018). DOI 10.1021/acs.nanolett.8b00083.
- [76] JCMsuite. <http://www.jcmwave.com> (2018).
- [77] Garcia Santiago, X., Zschiedrich, L., Burger, S. & Rockstuhl, C. *in preparation* (2018).

Acknowledgements

We acknowledge support by Freie Universität Berlin through the Dahlem Research School and by MINECO-FEDER, grants FIS2014-55563-REDC, and FIS2015-69295-C3-1-P. We thank Sven Burger for fruitful discussions and Xavier Garcia Santiago for his work on the Mie code and the algorithm for obtaining T -matrices from FEM simulations.